JARS Journal of Applied Remote Sensing

RESEARCH PAPER

Improved urban flood detection in deeper floods using synthetic aperture radar double-scattering intensity and interferometric coherence

David C. Mason[a,b,*] **and Sarah L. Dance**[a,b,c]
[a]National Centre for Earth Observation, Reading, United Kingdom
[b]University of Reading, Department of Meteorology, Reading, United Kingdom
[c]University of Reading, Department of Mathematics and Statistics, Reading, United Kingdom

ABSTRACT. Detection of flooding in rural areas is now commonly performed by high-resolution synthetic aperture radar (SAR) sensors. However, flooding in urban areas causes a greater risk to lives and property. Urban flood detection is more challenging due to SAR shadow, layover, and double scattering effects. Nevertheless, it may often be identified using the fact that in a post-flood image, double scattering between building walls and adjacent floodwater generally exceeds that in a pre-flood image, where double scattering occurs between buildings and adjacent ground. However, in the event of the urban region being deeply flooded, only a part of the building walls may remain above the flood level so that the post-flood double scattering may be reduced and a flooded region may be misclassified as non-flooded. We investigate whether flood detection can be improved for deeper urban floods using interferometric coherence as an adjunct to double scattering. An urban area that is not flooded should often exhibit high coherence between image pairs, whereas if there is flooding in one of the images the coherence should be low. An urban flood in Japan that contained deep-flooded, shallow-flooded, and non-flooded areas was used as a test example. It was imaged by Sentinel-1, and WorldDEM Digital Surface Model data was used to estimate flood depth and building orientation. An analysis of double scatterers of low post-/pre-flood brightness ratio was carried out for deeply flooded and non-flooded urban double scatterers. It was shown that using coherence, 58% of the deeply flooded buildings could be detected at the cost of a 16% false-positive rate. Without the use of coherence to supplement the brightness ratio, all these deeply flooded buildings would be misclassified as non-flooded. This finding could be of use in automating the detection of urban flooding as an aid to flood risk management.

Keywords: flood incident management; hydrology; synthetic aperture radar; interferometric coherence

Paper 240315SS received May 21, 2024; revised Sep. 25, 2024; accepted Oct. 4, 2024; published Nov. 9, 2024.

1 Introduction

Flooding from pluvial, fluvial, and coastal sources is a significant natural hazard in many parts of the world. The influences of climate change and growing urbanization in floodplains and coastal

*Address all correspondence to David C. Mason, d.c.mason@reading.ac.uk

Handling Editor: Zhaoyue Wu, Guest Editor of the Special Section on Intelligent Remote Sensing for Water Resources: Advances, Challenges and Perspectives

regions mean that flooding is likely to become more frequent and severe in the future, leading to an increased proportion of the population being exposed to floods.[1,2]

An important tool for operational flood incident management is a synoptic map of the extent of the flooding produced in near real-time.[3] Such flood extent maps can also provide data for assimilation into flood models to assist them in their predictions (e.g., Refs. 4 and 5) and for evaluation of flood inundation forecasting systems (e.g., Refs. 6–8). High-resolution synthetic aperture radar (SARs) are useful sources of flood extent maps as they have the ability to see through clouds and work at night as well as by day. The Sentinel-1 Global Flood Modeling (GFM) product now provides probabilistic flood extents in near real-time on a global basis.[9]

In rural areas where floodwater has no emergent vegetation or significant water turbulence, the SAR signal is specularly reflected away from the sensor by the water surface so that there is low backscatter. Automated flood detection in rural areas has been extensively researched and is reviewed in Refs. 10 and 11.

Even though the major portion of a flood may lie in rural areas, flooding in urban areas causes a greater risk to lives and property. While the side-looking nature of SAR tends to simplify automated flood detection in rural areas, it complicates it in urban areas. This is because it causes extensive strong double scattering that occurs between buildings and adjacent ground surfaces in urban areas. In addition, the presence of buildings results in radar shadow and layover, obscuring substantial areas of the urban ground surface from the SAR. Nevertheless, a variety of approaches to the problem have been studied, including the analysis of backscatter in a post-flood SAR image,[12–15] analysis of backscatter changes between pre- and post-flood SAR images,[16–21] use of interferometric coherence together with intensity backscatter in pre- and post-flood SAR images,[22–31] and multitemporal analysis of SAR images.[32–34]

This paper is concerned with the change detection approach, whereby urban flooding is detected by comparing a post-flood image acquired when the area is flooded to a non-flooded (pre-flood) image. The approach was first introduced in Ref. 16 to reduce over-detection in inundated urban areas.

As double scattering is the dominant SAR scattering mechanism in the urban area, a change detection method can be constructed using double scattering to discriminate between flooded and non-flooded areas.[16–21] This is because double scattering generated between suitably oriented buildings and adjacent floodwater in the post-flood image should generally exceed that generated from the buildings and adjacent non-flooded ground in the pre-flood image.

Thus, for an urban region subjected to shallow flooding compared with the building heights, if the post-/pre-flood brightness ratio is greater than 1, it is likely that the region is flooded, whereas if the brightness ratio is approximately equal to 1, the region is probably not flooded. However, in the less common scenario of an urban region being deeply flooded so that only a part of the building walls remains above the flood level, the brightness ratio may again reduce to 1, and a flooded region may be misclassified as non-flooded (see Sec. 3). This is a limitation of the double scattering brightness ratio method. Indeed, in the rare event that buildings are completely submerged, the brightness ratio becomes much less than 1, similar to a rural flood.

A number of change detection studies have considered the use of interferometric coherence as an adjunct to brightness ratio for detecting floods in urban areas.[22–31] An urban area that is not flooded should often show high coherence between post- and pre-flood images, whereas if there is flooding, the coherence should be low. These studies are reviewed in Sec. 2. While they have invariably shown improved classification of flooded/non-flooded urban areas compared with using double scattering alone, the particular case of deep flooding does not appear to have been investigated before. Interferometric coherence is likely to be particularly useful in this case, for which the brightness ratio has little discriminatory power.

The objective of the paper is to investigate whether the change detection method based on brightness ratio can be improved for deeper urban floods using interferometric coherence to assist the brightness ratio in discriminating flooded from non-flooded regions. The method was tested using as an example an extensive urban flood imaged by Sentinel-1 containing deep-flooded, shallow-flooded, and non-flooded areas to allow comparison between them. The testbed used was a change detection system developed to detect urban flooding on a global basis using 10-m resolution Sentinel-1 and 12-m resolution WorldDEM Digital Surface Model (DSM) data.[18] The Sentinel-1 constellation provides open-access, processed, geo-registered data in near real-time on

a global basis, thus is well-suited for flood detection. The DSM was used to estimate flood depth and building orientation for brightness ratio calculation.

The structure of the paper is as follows. Section 2 reviews relevant literature on the use of brightness ratio and interferometric coherence in urban flood detection. Section 3 discusses the theoretical background, including the dependence of the double scattering post-/pre-flood brightness ratio on the flood depth and other parameters, and the measurement of interferometric coherence. Section 4 introduces the study event and associated data sets. Section 5 describes the method involving the detection of double scatterers using the DSM. Section 6 gives the results and shows that over half of the deeply flooded buildings can be detected at the cost of a false-positive rate that is not too high. In Sec. 7, the results are discussed and we conclude that supplementing brightness ratio with interferometric coherence could be an important step in the process of automating the detection of urban flooding as an aid to flood risk management.

2 Use of Brightness Ratio and Interferometric Coherence in Urban Flood Detection

Several change detection studies have considered the use of interferometric coherence as an adjunct to (or replacement for) the brightness ratio for detecting floods in urban areas. Reference 22 investigated the role of coherence for detecting floodwater in agricultural and urban areas using COSMO-SkyMed images and showed that the use of coherence in urban areas allowed a considerable reduction in classification errors compared with using intensity data only. Reference 23 used strong double-scattering SAR returns from flooded buildings aligned roughly with the satellite flight direction to first detect the urban area. The urban flooding determined using SAR intensity was then refined using the change in coherence between pre- and post-flood SAR images. The method was tested using Sentinel-1 data from Hurricane Harvey in Houston, Texas, in 2017, with good results. Reference 24 employed unsupervised classification and a Bayesian network fusion framework to detect urban flooding using SAR intensity and coherence. It was shown that coherence provides valuable information in addition to intensity in urban flood mapping, again using Sentinel-1 data from Hurricane Harvey. For the same flood, Ref. 25 also used an active self-learning neural network applied to TerraSAR-X intensity and coherence information to perform urban flood mapping. Reference 26 tested numerous urban flood mapping approaches including change detection and coherence using Canadian flood events. Reference 27 studied urban flood detection in Indonesian floods using SAR intensity and coherence. Reference 28 combined the brightness ratio and coherence information into a single measure of urban flooding, and, using an unsupervised classification of Sentinel-1 data of an urban flood in Iran, showed that the urban flood measure gave improved classification compared with using the brightness ratio alone. Reference 29 enhanced the mapping of urban floodwater using both co- and cross-polarized SAR images to detect significant decreases in multitemporal InSAR coherence and considered not only double scattering but also multiple scattering from buildings. Reference 30 improved urban flood mapping by applying a deep convolutional neural network with an urban-aware model to dual-polarization Sentinel-1 multitemporal intensity and coherence data. Reference 31 mapped urban flooding using a deep learning convolutional Siamese network employing change detection and coherence. Other studies have investigated using coherence alone to detect urban flooding.[33–35] All these methods have illustrated the considerable discriminatory power of coherence for identifying urban flooding.

3 Theoretical Background

Double scattering caused by buildings may result from ground-wall or wall-ground scattering. The resulting return generally has high intensity not only because of the high proportion of the incoming radiation that is reflected to the sensor but also because the double scattering ray paths all have the same length, corresponding to the slant range of the base of the wall.[36] For co-polarized data, double scattering is strongest when the building wall is parallel with the satellite's direction of travel.[37]

Reference 18 summarized Ref. 17, which used double scattering to develop a method of local flooding level estimation in urban areas using VHR SAR images. They used the rationale

developed in Ref. 37 to associate the building wall height h above the ground or water surface to the contribution of the double scattering to the radar cross section σ^0 –

$$\sigma^0 = \mathrm{hf}(\mathbf{p}) \tag{1}$$

where $\mathbf{p}$ is a vector of known parameters and $\mathbf{p} = (l, \sigma, L, \varepsilon_w, \varepsilon_s, \theta, \varphi)$. Here, l is the building length; σ and L are the standard deviations and the correlation length of the stochastic process representing the ground surface, respectively; ε_w is the complex dielectric constant of the building wall; ε_s is the complex dielectric constant of the ground surface; θ is the SAR incidence angle; and φ is the angle between the wall and the satellite direction of travel.

In this study, we acquire a pre-flood and a post-flood intensity image. The ratio, r, of the calculated double scattering cross-section between the post- and pre-flood images is given by

$$r = \sigma_w^0/\sigma_g^0 = (h_\mathrm{A} - h_\mathrm{W}) f(\mathbf{p}_w)/((h_\mathrm{A} - h_\mathrm{G})\mathrm{f}(\mathbf{p}_g)). \tag{2}$$

In Eq. 2, we have assumed a water surface (σ_w^0) in the post-flood image and a ground surface (σ_g^0) in the pre-flood image. The building wall height is given by h_A, h_W is the height of the floodwater, h_G is the ground height, and $\mathbf{p}_w(\mathbf{p}_g)$ is $\mathbf{p}$ for water (ground).

To assess whether the ground around a correctly oriented building is flooded or not, it is usually assumed that the flood depth is small compared with the building heights. If the depth of flooding is small, Eq. (2) reduces to –

$$r \approx f(\mathbf{p}_w)/\mathrm{f}(\mathbf{p}_g). \tag{3}$$

From Eq. (3), if the ground is non-flooded, the ratio r should be 1. However, if the ground is flooded, $r > 1$, primarily because the permittivity of water is higher than that of asphalt (see Table 1 of Ref. 14). For an S-1 pixel, the ratio for a flooded building may be reduced due to the size of the pixel. However, it should still be greater than 1.

The ratio is a maximum $r_{\max}$ when the flooding is small and when $h_W \approx h_G$. If the building is flooded to a significant height, $h_W > h_G$ and $r < r_{\max}$. Figure 1 illustrates the effect of varying flood depth on the double scattering from a building. Figure 1(a) shows double scattering from the ground ($r = 1$) and Fig. 1(b) double scattering from a low flood depth ($r > 1$). When the flood depth is equal to the building height [Fig. 1(c)], there is no longer any double scattering, and the backscatter reduces to the level σ_r^0 generally associated with a rural flood ($r < 1$). It follows that there is a flood depth between these two cases where the backscatter is similar to that in the non-flooded case (a), when $r = 1$ [Fig. 1(d)]. In real situations, the backscattering may be more complicated because of adjacent buildings.

Note that theoretical studies estimating the brightness ratio r for HH-polarized data found that it was high at $\varphi = 0$ deg but only small at $\varphi > 10$ deg,[22] which implies that few double scatterers might be detected in an urban area, which would limit the effectiveness of the method. However, recently, it has been shown that for Sentinel-1 VV data, the modeling underestimates the number of double scatterers with high brightness ratios in the φ range of 10 deg to 30 deg.[38]

In this study, the interferometric coherence is used as an additional feature to assist with the discrimination of flooded and non-flooded double scatterers. The interferometric coherence at a point is computed from N samples neighboring the point taken from a pair of complex SAR images, S_1 and S_2, and is expressed as –

$$\gamma = \frac{\left| \sum_{i=1}^{N} S_{1\mathrm{i}} S_{2\mathrm{i}}* \right|}{\sqrt{\left(\sum_{i=1}^{N} |S_{1\mathrm{i}}|^2 \sum_{i=1}^{N} |S_{2\mathrm{i}}|^2 \right)}}. \tag{4}$$

The coherence varies in the range [0, 1], with 1 indicating fully correlated data and 0 fully uncorrelated data. In urban areas, two images with the same SAR parameters taken before the flood (pre-event pair) will generally exhibit high coherence as there will be little change between them. By contrast, if flooding is present in one of the images (co-event pair), coherence will generally be low because the changes between the images result in decorrelation. In practice, the coherence of the pre-event pair may be reduced somewhat due to anthropogenic changes between the images caused, for example, by differing traffic conditions. To compensate for this, a coherence ratio may be taken between the co-event and pre-event pair coherences, and the

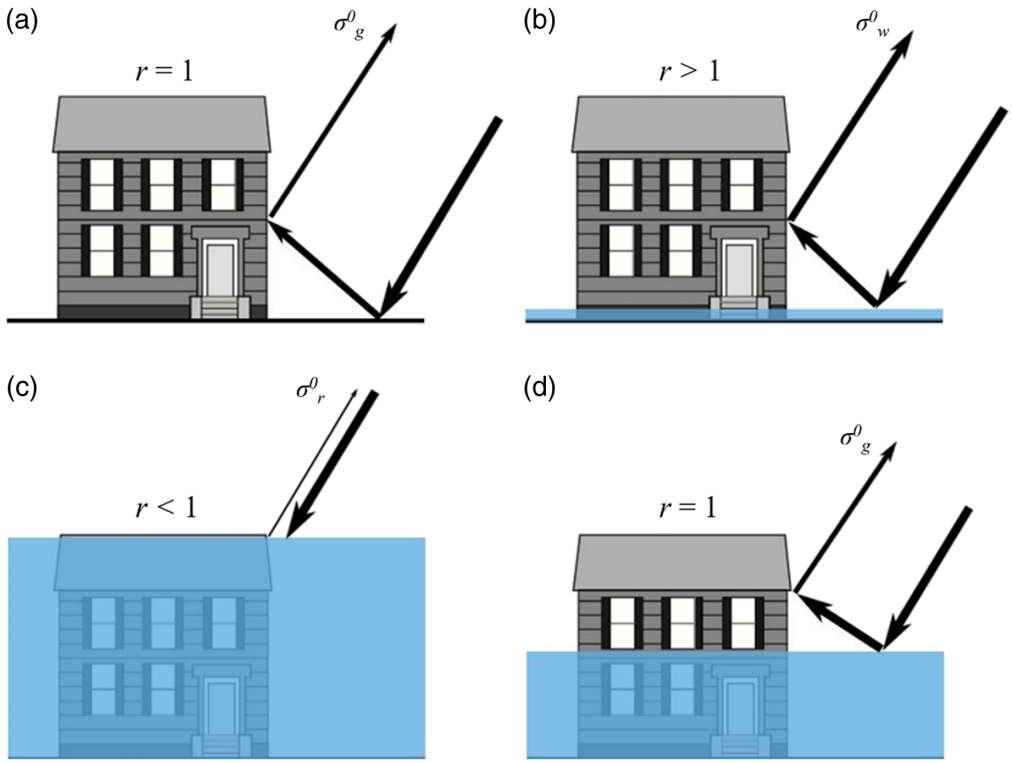

Fig. 1 Effect of flood depth on the double scattering brightness ratio (r) from a building. (a) Double scattering from the ground, (b) double scattering from a low flood depth, (c) backscattering (σ^0_r) when a building is completely inundated, and (d) double scattering from a significant flood depth at which backscatter intensity is equal to the case shown in panel (a) (after Ref. 35).

coherence ratio used to discriminate between flooded and non-flooded urban areas.[28] Unlike double scattering, coherence is independent of the orientation of buildings.[39] Note however that coherence is a local area measure centered on a pixel, whereas the brightness ratio is pixel-based and therefore has a higher spatial resolution.

The method employed here requires three Sentinel-1 images $t1$, $t2$, and $t3$ of the same pass and incidence angle, where $t1$ and $t2$ are acquired before flooding and image $t3$ is acquired during flooding. The double scattering cross-section ratio r is

$$r = \sigma^0_{t3}/\sigma^0_{t2}, \tag{5}$$

and the interferometric coherence ratio coh_rat ($0 < coh\_rat \leq 1$) is

$$coh\_rat = \gamma_{t2t3}/\gamma_{t1t2}, \tag{6}$$

where σ^0_{t3} and σ^0_{t2} are the backscattering cross-sections (linear scale) of images $t3$ and $t2$, respectively; γ_{t2t3} and γ_{t1t2} are the coherences between images $t2$ and $t3$ (co-event pair), respectively; and $t1$ and $t2$ (pre-event pair).

4 Study Event and Data Sets

The method was tested using as an example the urban flooding in the city of Koriyama in Japan that occurred due to Typhoon Hagibis on October 12 to 13, 2019. The flooding included an area of deep urban flooding as well as areas of shallow flooding and non-flooded areas, allowing the scenarios to be compared. Typhoon Hagibis carried with it a large volume of warm air, resulting in unprecedented rainfall across a third of Japan.[40] The typhoon was extremely strong and affected a vast area, generating heavy rain, storms, high waves, and storm surges. In Japan, the total damage caused was calculated to be 15 billion USD. It has been estimated that thousands of buildings were flooded in Koriyama itself.[41]

A flood reference map of the extent of the flooding in Koriyama was published by the Geospatial Information Authority of Japan (GSI) from the information collected up to October 13 (Fig. 2).[42] The map was developed using aerial images and elevation data. The main urban region flooded in Koriyama was to the east of the Abukuma river, between this river and a tributary. The flooding was imaged by Sentinel-1 (descending pass) on October 12, 2019 (Table 1).

Figure 3 shows an aerial photograph of the flooding, viewed from the east, taken on the morning of October 13 just a few hours after the SAR overpass.[43] It is apparent that the north of the flooded region contains more factories than housing, whereas the south contains more

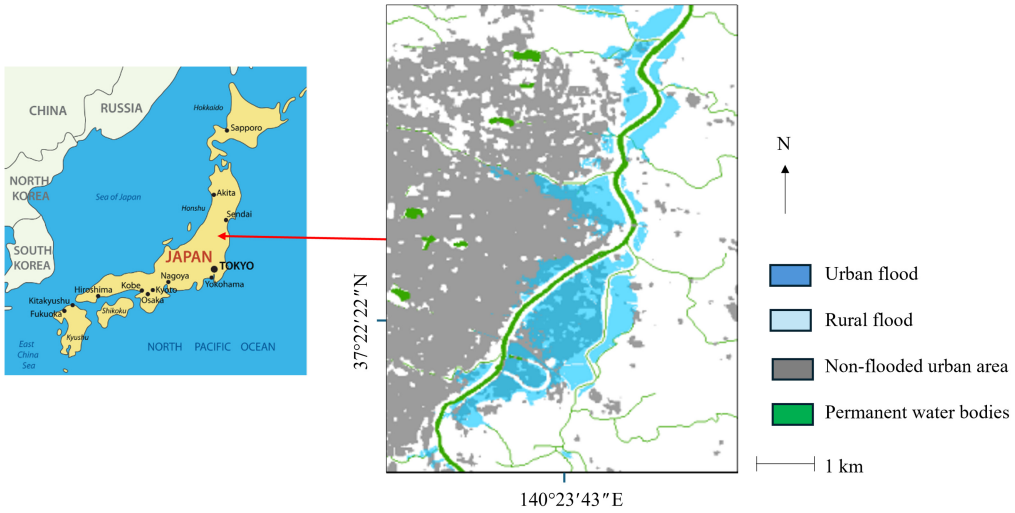

Fig. 2 Reference flood map of the Abukuma river flood (Abukuma river runs south to north).[42]

Table 1 Sentinel-1 IW VV/VH images used for flood detection (UTC = coordinated universal time).

Data type	Post-flood image acquisition time (UTC)	Pre-flood image acquisition time (UTC)
Intensity (GRD images)	October 12, 2019, 20:42 UTC	October 6, 2019, 20:43 UTC
Coherence (SLC images)	October 12, 2019, 20:42 UTC	October 6, 2019, 20:43 UTC
		September 24, 2019, 20:43 UTC

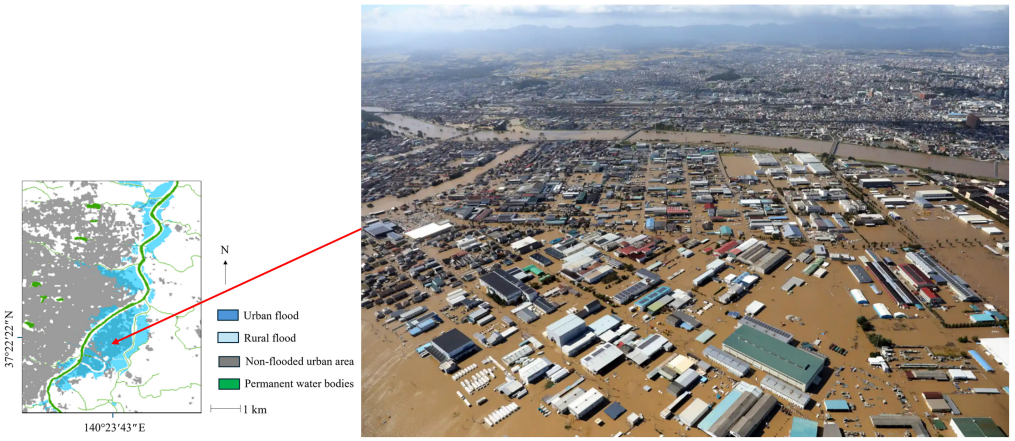

Fig. 3 Aerial photograph of the flooding viewed from the East.[43]

housing. Also, the buildings in the north often seem flooded quite deeply compared with those in the south.

The Koriyama flood is a rare example of a deep flood over a large urban area that has been imaged by *S*-1 and for which validation data exists. The area of deep flooding covers several square kilometers and includes hundreds of flooded buildings. As a result, there are hundreds of individual scenarios of lower buildings and higher buildings at different orientations in deep floodwater, with associated double scattering and coherence measurements. Analysis of Google Earth images of the deep-flooded region shows that the buildings are mostly surrounded by asphalt and that most of the buildings are built of brick. This is similar to many urban areas around the world, as asphalt surrounding brick-built buildings is very common.

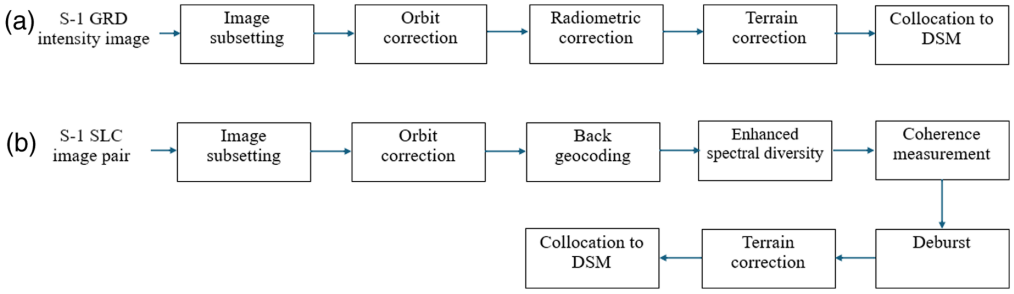

Fig. 4 Pre-processing steps applied to the *S*-1 images. (a) *S*-1 GRD intensity image pre-processing. (b) *S*-1 SLC image pair pre-processing to estimate coherence.

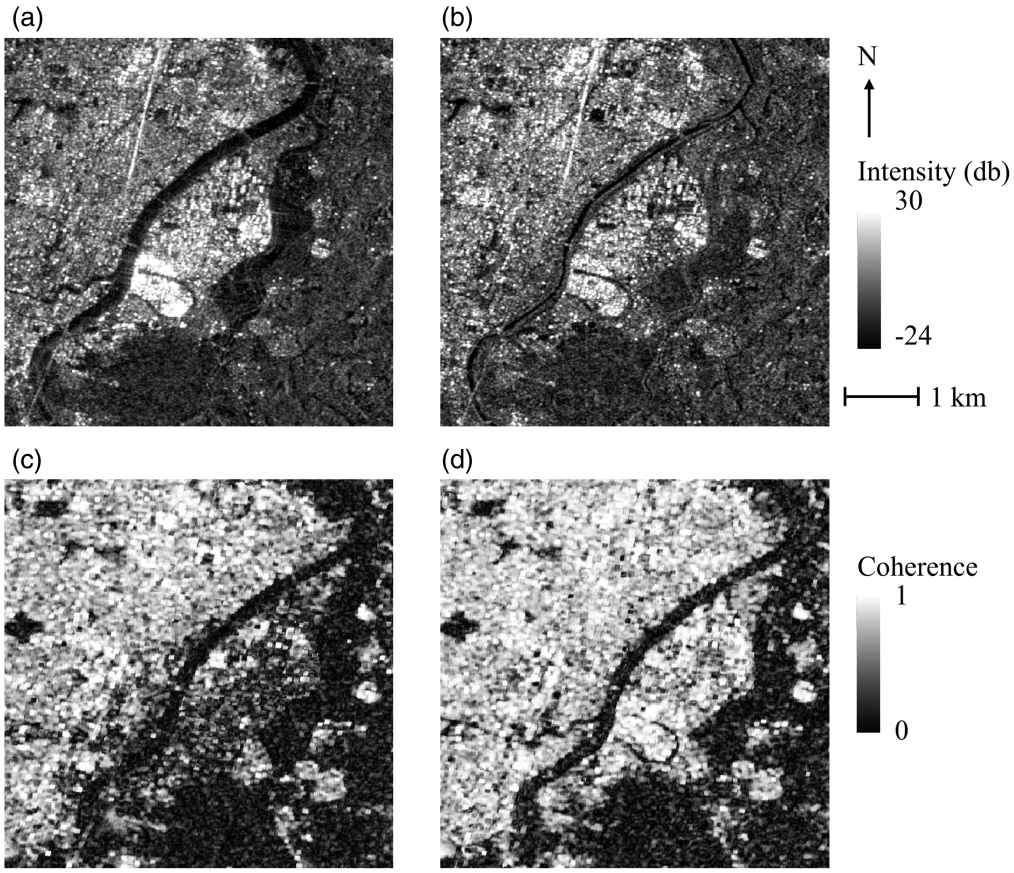

Fig. 5 (a) S-1 VV intensity image for October 12, 2019 (post-flood). (b) S-1 VV intensity image for October 6, 2019 (pre-flood). (c) Coherence image for co-event image pair October 12, 2019, and October 6, 2019. (d) Coherence image for pre-event image pair October 6, 2019, and September 24, 2019.

A number of preprocessing steps were applied to the SAR images using the European Space Agency (ESA) SNAP toolbox (Fig. 4). For the Ground Range-Detected (GRD) intensity images, the preprocessing steps to extract backscatter intensity included image subsetting, orbit correction, radiometric calibration, and range-Doppler terrain correction. The resulting post- and pre-flood intensity images were collocated to the DSM in the WGS84 coordinate system [Fig. 4(a)].

The Single-Look Complex (SLC) images were processed to extract image coherence as described in Ref. 44 [Fig. 4(b)]. The processing sequence on each image pair included image subsetting, orbit correction, back geocoding, enhanced spectral diversity, coherence measurement (using an 80-m square window), deburst, and range-Doppler terrain correction. In one pair, the image on October 6, 2019, was the master and the image on October 12, 2019, was the slave; in the other pair, the image on September 24, 2019, was the master and the image on October 6, 2019, was the slave. Each pair was then collocated to the DSM.

Figure 5 shows the *S*-1 VV post-flood (October 12, 2019) and pre-flood (October 6, 2019) intensity images, and the coherence images for the co-event image pair (October 12, 2019, and October 6, 2019) and pre-event pair (October 6, 2019, and September 24, 2019).

The World Settlement Footprint (WSF) 2019 10-m resolution dataset was used to identify the Koriyama urban area. The WSF mask is open-access data available on ESA's Urban Thematic Exploitation Platform (U-TEP).[45] Only VV polarization data were used, as previous results have indicated that VV polarization is better than VH at distinguishing flooded from non-flooded double scatterers.[38]

5 Method

A supervised approach was adopted based on detecting double scatterer (DS) pixels in the urban area that were aligned roughly parallel to the satellite track and determining whether these DS were flooded or non-flooded using the flood reference map. The processing steps involved are shown in Fig. 6.

Following Ref. 18, we use a Roberts edge detector[46] to detect strong edges in the DSM (mainly corresponding to building edges). The edge detector calculates the local gradient at a pixel using a 2×2-pixel window centered on the pixel. The Roberts detector is used because the width of streets in dense urban areas may be comparable to the DSM pixel size. Other edge detectors typically have a larger kernel (e.g., Sobel) and would not be appropriate. Edges with a large aspect angle to the satellite direction of travel ($\varphi > 35$ deg) are suppressed, as the SAR image is unlikely to exhibit substantial double scattering at these edges. Non-maxima suppression is performed on these edges. Due to the fact that the aspect angle calculated can be rather noisy, selected pixels are also required to have a backscatter above a threshold in the pre-flood image. The rationale behind this is that a correctly oriented double scatterer should give a reasonably sized backscatter even in the pre-flood image.

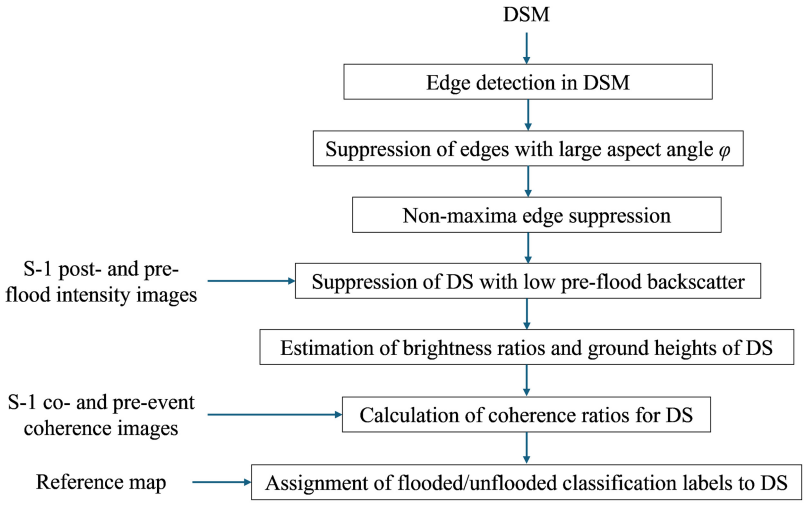

Fig. 6 Processing steps in the identification and classification of double scatterers.

At each edge pixel, the pixel and its immediate neighbors on either side of it along a line perpendicular to its edge direction are selected. By examining these three pixels, we find the maximum brightness ratio between the post-flood and the pre-flood image, the maximum DSM height (assumed to be from a building roof), and the minimum DSM height. The minimum height is required to be in the height range expected for flooding. This reduces outliers from heights above reasonable flood levels. We assume that the minimum height is the local ground height, where the DSM and the DTM coincide. Hence, there is no need to generate a separate DTM from the DSM prior to the processing.

A DS is assigned to be wet or dry depending on its class in the corresponding position in the Koriyama flood reference map. The coherence ratio *coh_rat* is also calculated for each DS. Note that *coh_rat* is an areal measure from an 80-m square region centered on the DS, whereas the brightness ratio is that at the DS pixel itself.

6 Results

This section begins with the estimation of flood depths over the flooded urban area (Sec. 6.1). This is used in an analysis of DS brightness and coherence ratios in shallow-, deep-, and non-flooded urban areas. The question of how the coherence ratio can assist with discrimination of deep- and non-flooded DS of low brightness ratio is addressed (Sec. 6.2). The change in classification accuracy of DS of all brightness ratios when coherence is taken into account is also measured (Sec. 6.3), as is the change in accuracy of the urban flood extent (Sec. 6.4).

6.1 Estimation of Urban Flood Depths

The flood reference map of Fig. 2 was used in conjunction with the DSM of the area (Fig. 7) to develop an approximate urban flood depth map at the time of the SAR overpass. An approximate estimate of the flood depth in the region of deep flood D (Fig. 7) was made as follows. An analysis of the flood edge from the post-flood SAR image intersected with the DSM in the rural area east of Koriyama (in region DH) near region D gave an average rural flood edge height of 227.4 ± 0.2 m. The calculation was made over an area of gently sloping fields so that heights could be measured accurately. Almost 70% of the DS in region D have a ground height of less than 227 m, the mean DS ground height being 225.3 m (standard deviation = 1.1 m).

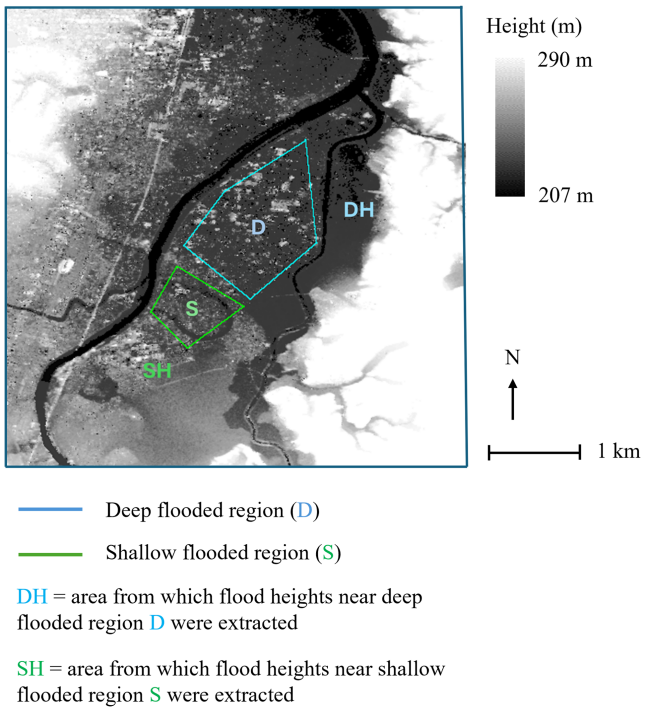

Fig. 7 DSM of the area containing the main flooded region in Koriyama, with deep and shallow-flooded regions demarcated.

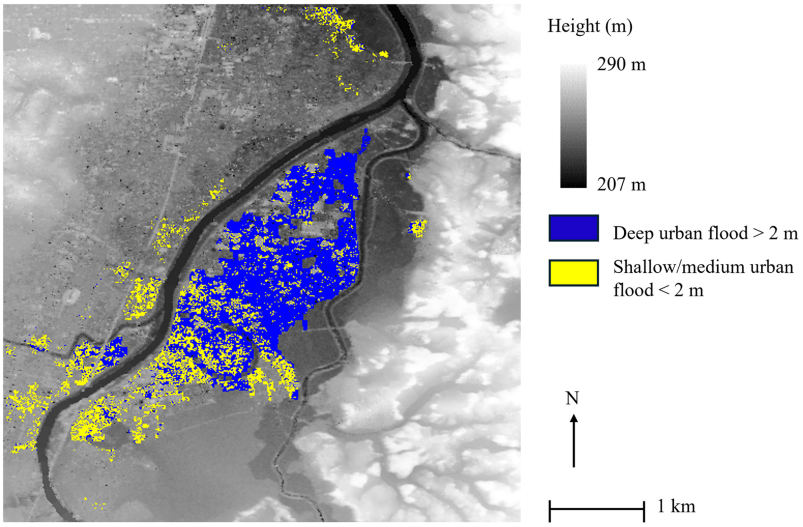

Fig. 8 Approximate flood depth map over the flooded urban area.

Assuming that the flood height does not change between regions D and DH, this gives a mean flood depth for these DS of 2.1 m, which is reasonably deep. About 30% of DS in region D have ground heights lower than 225.3 m and are flooded more deeply.

An approximate estimate of flood depth in the shallow flood region S (Fig. 7) was made in a similar fashion. An analysis of the post-flood SAR image flood edge intersected with the DSM in region SH near region S in a region of low slope gave an average flood edge height of 229.0 ± 0.1 m. The mean ground height of DS in region S is 228.5 ± 0.2 m, giving a flood depth in region S of 0.5 ± 0.2 m. This analysis indicates that region S is an area of shallow flooding, whereas region D is flooded more deeply. Between regions SH and DH, there was a slight fall in flood elevation of 1.6 m over a distance of 2 km. Figure 8 shows the approximate flood depth map over the whole flooded urban area developed using a flood-fill to the flood level in the shallow flood area.

This finding is corroborated by the study carried out by the Japanese firm Synspective, which analyzed the flood damage in Koriyama around the Abukuma river using Sentinel-1 data observed on October 12, 2019 (the same post-flood image as used in the present study).[41]

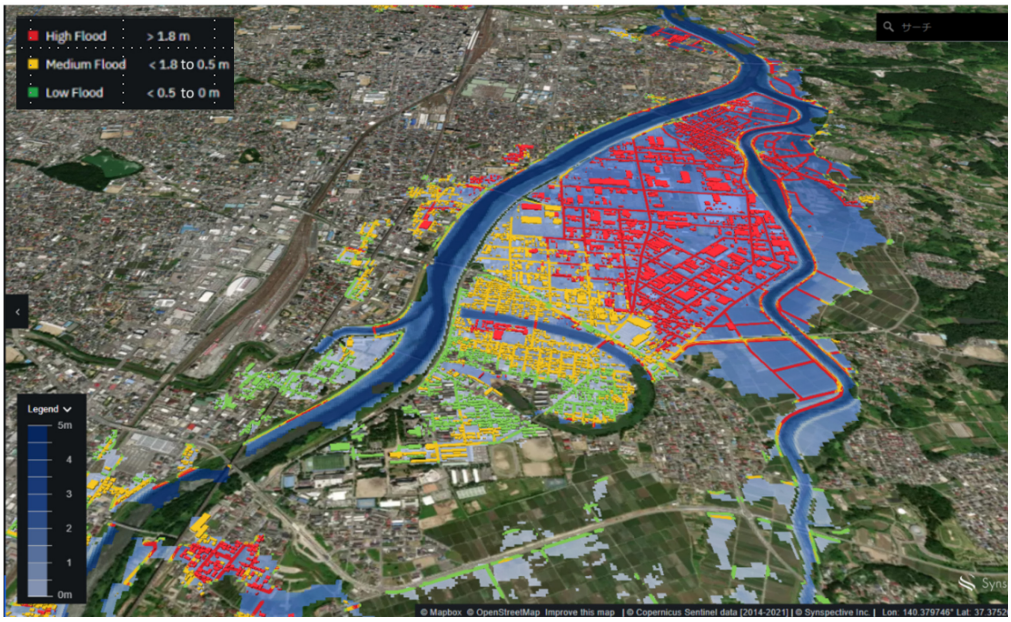

Fig. 9 Synspective analysis of the Abukuma river flood.[41]

Synspective found an area of shallow to medium flooding (<1.8 m) roughly corresponding to region S and an area of deeper flooding (>1.8 m) roughly corresponding to region D (Fig. 9). These areas also seem to be apparent in the aerial photo (Fig. 3).

6.2 Analysis of DS Brightness and Coherence Ratios

Figure 10(a) is a scatter plot of brightness ratio r versus coherence ratio for DS in the shallow-flooded, deep-flooded, and non-flooded urban areas of Koriyama. The numbers of counts in each class have been kept similar. The lowest number is in the shallow flooded class so other classes have been subsampled. Figure 10(b) shows brightness ratio histograms generated from Fig. 10(a).

Table 2 shows the class brightness ratio and coherence ratio means and standard deviations. It is apparent that the mean brightness ratio for the deep-flooded class is quite high (6.0), though

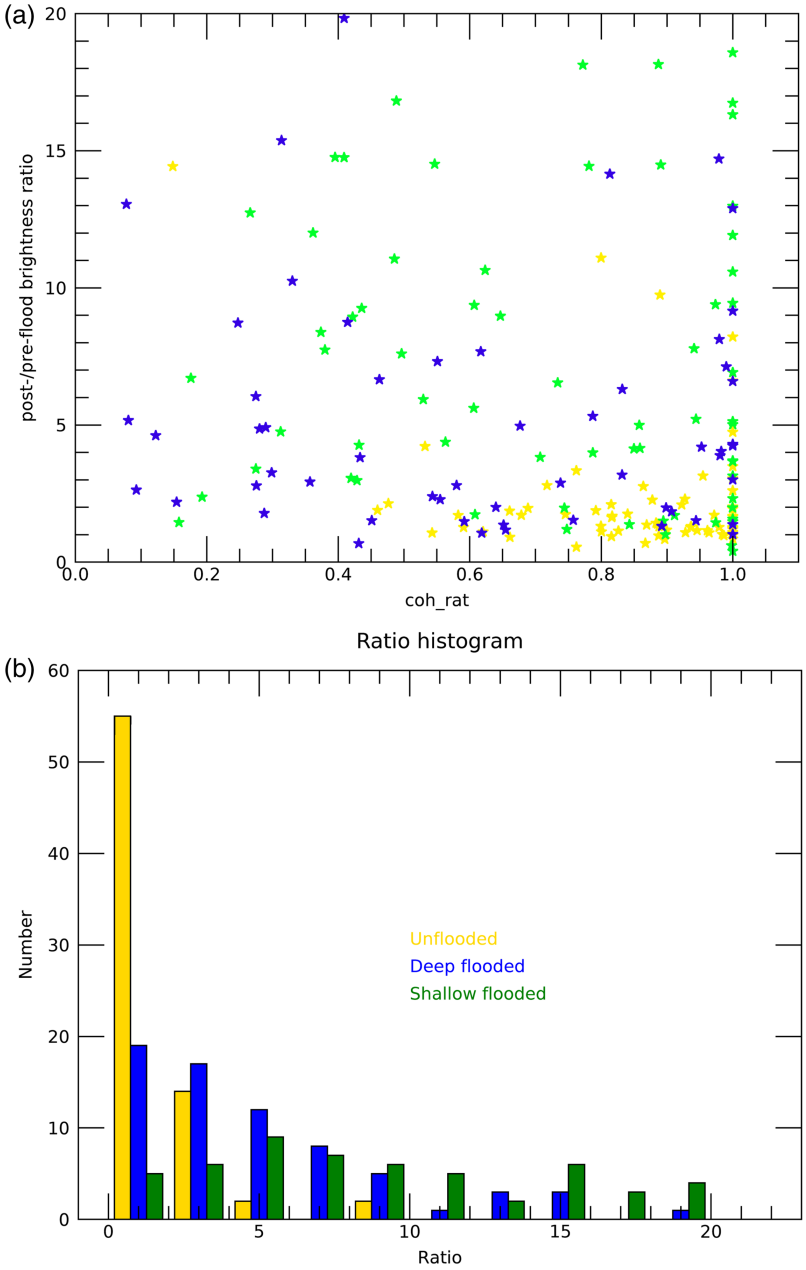

Fig. 10 (a) Scatter plot of double scatterers in shallow-flooded, deep-flooded, and non-flooded areas of Koriyama (blue = deep flood, green = shallow flood, yellow = non-flooded). (b) Brightness ratio histograms generated from panel (a).

Table 2 Class brightness and coherence ratio means and standard deviations.

Class	Number of DS	Mean (s. dev.) brightness ratio *r*	Mean (s. dev) coherence ratio *coh_rat*
Shallow-flooded	66	13.4 (10.9)	0.69 (0.28)
Deep-flooded	71	6.0 (7.4)	0.65 (0.30)
Non-flooded	73	1.8 (1.5)	0.88 (0.13)

with a large standard deviation (7.4). This is likely because of the mix of building heights that occur in region D (Fig. 7). The mean building height associated with the DS in this region is 3.8 m, though the standard deviation is large at 2.6 m due to a number of taller buildings. The higher buildings generate higher r values, though there are other lower buildings flooded more deeply for which r is lower. The depth of flooding of some of the lower buildings is apparent by comparing them to the taller buildings in the aerial photo (Fig. 3), which was acquired only a few hours after the SAR overpass.

Note that the shallow flood class has a higher mean brightness ratio (13.4) than the deep flood class, which is as expected given the lower depth of flooding in region S and the fact that there are many buildings of similar height in regions S and D. The mean building height associated with the DS in region S is 3.2 m, lower than in region D, but the much smaller standard deviation (1.6 m) indicates a more uniform building height in region S.

Meanwhile, the non-flooded class has a lower mean brightness ratio (1.8) than the deep-flooded class, though the histograms of these classes in Fig. 10(b) show there are many deep-flooded DS at low ratios, and it appears that the deep flood class mean ratio has been raised by higher buildings.

Regarding the coherence ratio *coh_rat*, the mean of this is lower for the two flooded classes than the non-flooded class, as expected. From Fig. 10(a), it is apparent that some flooded DS have *coh_rat* = 1.0, which appears to be due to the coherence from the pre-event image pair $t1$ and $t2$ being low and similar to the coherence from the co-event image pair $t2$ and $t3$.

A further interesting fact is that the brightness ratio and coherence ratio turn out to have only limited dependence. Analysis of the data used here indicates that the correlation between r and *coh_rat* is −0.005 only.

Our aim is to examine how well coherence can assist with the discrimination of deep-flooded and non-flooded double scatterers when these have a low brightness ratio. Figure 11 shows coherence ratio histograms for low brightness ratio DS ($r < 2$) for the deep and non-flooded classes. These DS samples are those for which the brightness ratio has low discriminatory power

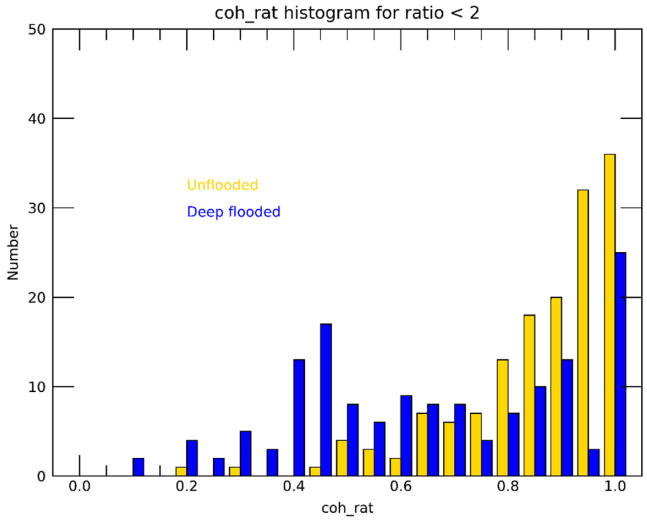

Fig. 11 Coherence ratio histograms for low brightness ratio double scatterers ($r < 2$), for deep-flooded and non-flooded classes.

for urban flood detection. All DS samples in the deep-flooded class have been used, together with a similar size subsample from the non-flooded class. Table 3 shows coherence ratio means and standard deviations for these low brightness ratio DS for these classes. For the deep-flooded DS, a peak at low coherence ratio values around 0.4 to 0.5 is apparent, though there is a large spread including samples with *coh_rat* = 1.0. The non-flooded DS generally have high *coh_rat* values, with a strong peak at *coh_rat* = 1.0.

A ROC (receiver operating characteristic) curve analysis was used to identify an optimum threshold for *coh_rat* (Fig. 12).[47] A ROC curve plots the true-positive rate (TPR, recall) against the false-positive rate (FPR) at each threshold setting. It is the cumulative distribution function (CDF, area under curve from 0 to threshold) of the detection probability on the *y*-axis versus the CDF of the false probability on the *x*-axis. The higher the area under the curve (AUC), the better the model is at distinguishing deep-flooded from non-flooded DS.

The optimum threshold for *coh_rat* (*coh_rat* ≤ *coh_rat_thr*) was chosen as the value that minimizes the sum of squares of (1-TPR) and FPR. Table 4 gives the optimum coherence ratio threshold *coh_rat_thr*, and corresponding true- and false-positive rates, for a number of different values of the brightness ratio threshold *ratio_thr*. The highest value of AUC occurred for *ratio_thr* = 2.0, for which TPR = 0.58 and FPR = 0.16. The AUC value of 73% lies in the range deemed acceptable.[47] We found that *coh_rat_thr* was 0.70, independent of *ratio_thr*.

Table 3 Coherence ratio means and standard deviations for low brightness ratio DS and for deep-flooded and non-flooded classes.

Class	Number of DS	Mean (s. dev.) coherence ratio *coh_rat*
Deep-flooded	147	0.68 (0.24)
Non-flooded	151	0.88 (0.14)

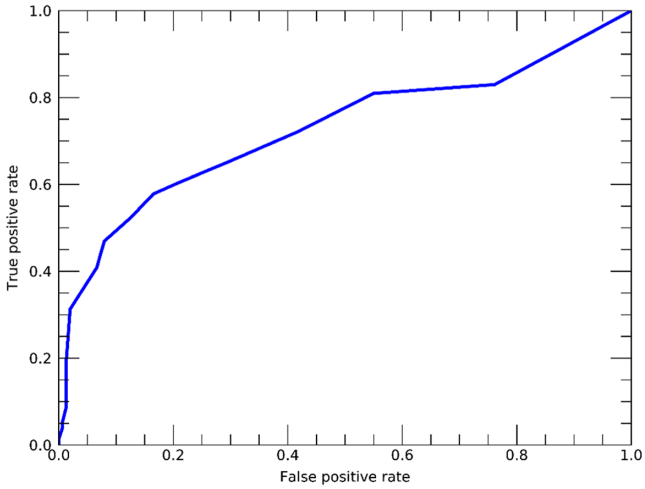

Fig. 12 ROC curve for brightness ratio threshold (*ratio_thr*) = 2.

Table 4 Optimum coherence ratio thresholds, and corresponding true- and false-positive rates, for different brightness ratio thresholds.

Brightness ratio threshold (*ratio_thr*)	Optimum coherence ratio threshold (*coh_rat_thr*)	True-positive rate (TPR)	False-positive rate (FPR)	Area under curve (AUC) %
2.5	0.70	0.57	0.16	72
2.0	0.70	0.58	0.16	73
1.5	0.70	0.56	0.14	71

The ROC analysis shows that a reasonable detection rate of deeply flooded buildings can be achieved for a false-positive rate that is not too high. If a lower false-positive rate is required, a *coh_rat_thr* of 0.60 gives a TPR of 0.47 and an FPR of 0.08, for example. If the coherence ratio was not being used to supplement the brightness ratio, all these deeply flooded buildings would be misclassified as non-flooded.

Because there is a small negative correlation between r and *coh_rat*, the use of the coherence ratio in conjunction with the brightness ratio should also increase the separation of flooded from non-flooded DS for DS having brightness ratios above *ratio_thr*. In this case, it turned out that only 25% of DS samples in the brightness ratio range $2 < r < 4$ were non-flooded, and there remained a significant fraction (25%) of flooded DS that had *coh_rat* = 1.0. Consequently, there would be no gain in setting a separate coherence ratio threshold for the brightness ratio range $2 < r < 4$.

As a result, a rule that can be used to classify a DS sample with brightness ratio r, coherence ratio *coh_rat*, is –

$$(r > ratio\_thr) | ((r \leq ratio\_thr) \,\&\, (coh\_rat \leq coh\_rat\_thr)) = \begin{cases} \text{TRUE}, & \text{flooded} \\ \text{FALSE}, & \text{unflooded} \end{cases}. \tag{7}$$

Figure 13 illustrates the discriminatory power of the coherence ratio for DS of low brightness ratio, for DS within the gold square in Fig. 13(a) overlaying part of the deep-flooded area D of

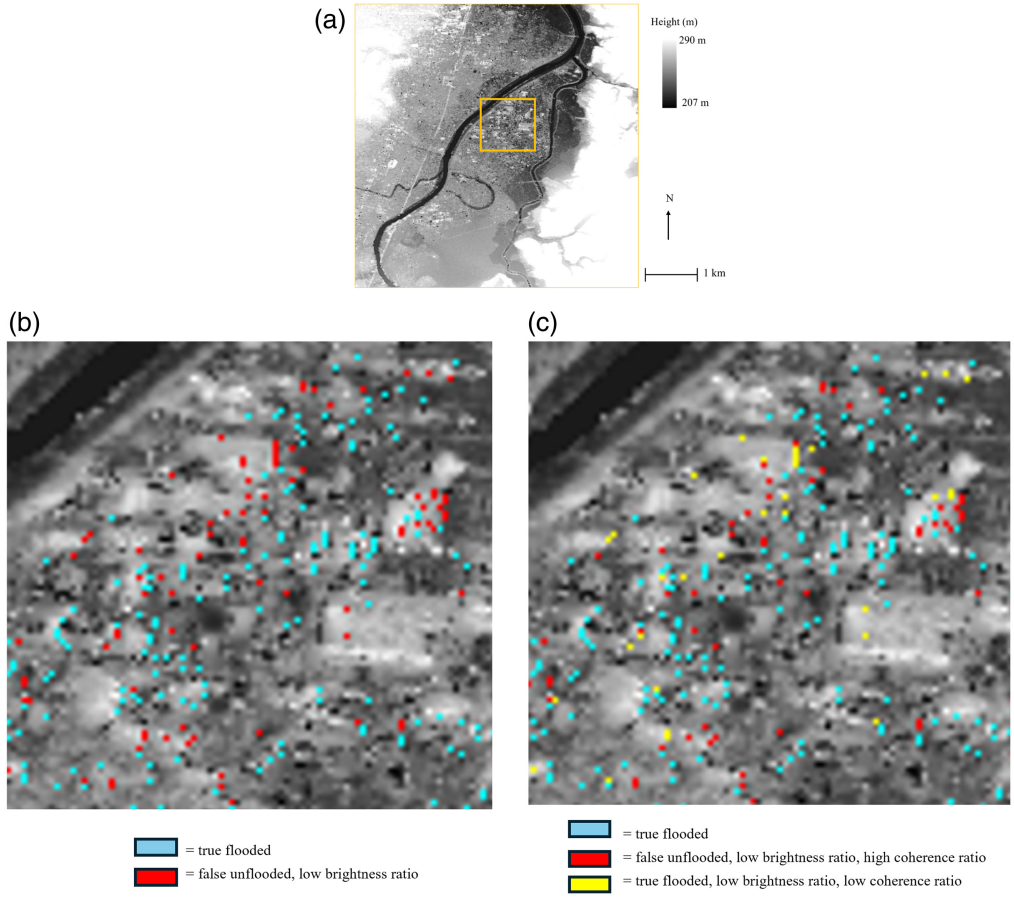

Fig. 13 Illustration of the discriminatory power of the coherence ratio for DS of low brightness ratio. (a) DSM of Koriyama with gold square overlaying part of the deep-flooded area D of Fig. 7. (b) DSM within gold square overlain with DS classified using brightness ratio but not coherence ratio. The DS are generally at the *E* of buildings as the SAR is looking *W* on a descending pass. (c) DSM within gold square overlain with DS classified using brightness ratio and coherence ratio. The discriminatory power of the coherence ratio is apparent compared with panel (b).

Fig. 7. Figure 13(b) shows DS classified into true flooded (cyan) and false non-flooded (red) using brightness ratio but not coherence ratio. The DS are generally at the Eastern edges of buildings as the SAR is looking West on a descending pass. Figure 13(c) shows that by classifying DS using coherence ratio as well as brightness ratio (using *coh_rat_thr* = 0.6), those DS of low brightness ratio and low coherence ratio can be classified as true flooded (yellow), rather than being misclassified as non-flooded (red) as in Fig. 13(b).

6.3 Change in Classification Accuracy of DS of All Brightness Ratios

The accuracy results given above have been limited to the classification of DS of low-intensity ratio that can be identified as flooded by having a low coherence ratio. It has been shown that many of these can be detected as flooded rather than being misclassified as non-flooded while misclassifying a few non-flooded DS as flooded.

There is also the wider question of the change in classification accuracy of DS samples of all brightness ratios in the deep-flooded and non-flooded areas using the coherence ratio as well as the brightness ratio (shallow-flooded DS classifications are not affected). In this case, any improvement in accuracy achieved for flooded lower buildings will be diluted somewhat because of the presence of the numerous taller buildings in the flood. These will not have a low brightness ratio and will be detected as flooded irrespective of their coherence ratio so that any increase in accuracy will be scenario-specific, whereas if all the buildings in a deep-flooded area were of low height the coherence test would improve the overall accuracy more. Notwithstanding this proviso, it was felt important to examine change in accuracy over the deep-flooded and non-flooded areas, and this is discussed below.

The metrics of accuracy, recall, and precision were used to assess how well a classification of DS performed.[48] Accuracy is the fraction of predictions made by a model that were correct. In this case of binary classification, the accuracy of DS classification = (TP + TN)/(TP + TN + FP + FN), where TN = true positive, TN = true negative, FP = false positive, and FN = false negative. Recall measures the proportion of true positives that were identified correctly (recall = TP/(TP + FN)). Meanwhile, precision measures the proportion of positive identifications that were actually correct (precision = TP/(TP + FP)).

Table 5 shows the confusion matrix giving the classification of DS using brightness ratio but not coherence ratio. The matrix was constructed using all the DS samples from the deep-flooded area and an equal number of DS samples from the non-flooded area (by limiting the height range of the non-flooded DS). A DS sample was classified as flooded if its brightness ratio r was greater than *ratio_thr*, else it was non-flooded. For this classification, the overall accuracy was 0.71, the recall 0.70, and the precision 0.71.

By contrast, Table 6 shows the confusion matrix giving the classification of DS using brightness ratio and coherence ratio, using *coh_rat_thr* = 0.6. The rule used to classify a DS sample is given in Eq. (7).

Table 5 Classification of DS using brightness ratio but not coherence ratio.

	Actual flooded DS	Actual non-flooded DS
Predicted flooded DS	347	143
Predicted non-flooded DS	147	358

Table 6 Classification of DS using brightness ratio and coherence ratio.

	Actual flooded DS	Actual non-flooded DS
Predicted flooded DS	407	165
Predicted non-flooded DS	87	336

For the classification based on coherence ratio as well as brightness ratio, the accuracy was 0.75, the recall 0.82, and the precision 0.71. Thus, using the new rule, the classification accuracy of DS samples increased from 0.71 to 0.75. For the non-flooded DS, their recall fell from 0.71 to 0.67 due to the increased false alarms. But this was more than offset by the increase in recall of the deep-flooded DS, which rose from 0.70 to 0.82. We conclude that the use of coherence has a positive effect also for this wider classification.

6.4 Change in Classification Accuracy of Urban Flood Extent

Another valid question to ask is, how does the reclassification of DS in the deep-flooded region affect the accuracy of the overall urban flood extent generated from DS heights? It must be borne in mind that any improvement in accuracy achieved for flooded lower buildings will be diluted in this case also, not only because of taller buildings in the flood but also because DS in the shallow-flooded as well as the deep-flooded region will influence the flood extent.

The unsupervised method of generating a flood extent described in Ref. 18 (briefly summarized here) was used to investigate this. A set of DS is chosen that is likely to be mainly flooded [i.e., TRUE according to Eq. (7)], together with another set whose members are likely mainly unflooded [FALSE in Eq. (7)]. Each member of the first set must be spatially close to a member of the second set and vice versa. This ensures that the flooded DS chosen are near the flood edge so that their flood depths are likely to be shallow, as required by Eq. (3). To reduce noise, the average height of the DS in each set is estimated. The local floodwater elevation is chosen as the mean of the flooded and unflooded average heights. Assuming a uniform floodwater elevation, pixels in the urban area with DTM heights less than the floodwater elevation are regarded as flooded; otherwise, not. The flood extent so produced is compared with the urban flooding in the validation image (Fig. 2) to estimate its accuracy.

Flood extents were produced for two scenarios, one using brightness ratio and coherence ratio and classifying DS according to Eq. (7) and the other using brightness ratio only. The flood extent using brightness ratio and coherence ratio was slightly more accurate (87.2%), but the improvement was very small. This is probably because (a) there were many more DS in both shallow- and deep-flooded regions (560 DS) than were reclassified from false unflooded to true flooded using the coherence ratio in the deep-flooded region (73 DS), and (b) many of the DS flooded/unflooded pairs were sited around the flood edge in the shallow-flooded region, which is ~1 km away from the reclassified DS in the deep-flooded region. In this case, we conclude that the use of coherence has little effect.

7 Discussion and Conclusions

Double scattering from appropriately oriented buildings in urban areas is a powerful means of discriminating flooded from non-flooded buildings if the flooding is not too deep. However, in the case of deep flooding, misclassification may often be avoided using image coherence. The aim of this study has been to investigate how much discrimination in such cases can be improved using the coherence ratio as an additional feature to supplement the brightness ratio. The flooding in Koriyama caused by Typhoon Hagibis has been used as a test case.

An analysis of DS of low brightness ratio has been carried out for deeply flooded and non-flooded urban DS. It has been shown that over half (0.58) of the deeply flooded buildings could be detected at the cost of a false-positive rate that was not too high (0.16). In case the false-positive rate needed to be reduced, halving the false-positive rate (to 0.08) still meant that almost half (0.47) of the deeply flooded DS of low brightness ratio could be detected. Without the use of the coherence ratio to supplement the brightness ratio, all these deeply flooded buildings would be misclassified as non-flooded. However, as the brightness ratio of DS increased, double scattering became the dominant discriminant feature compared with coherence.

On the wider question of the change in classification accuracy of DS samples of all brightness ratios in the deep-flooded and non-flooded areas using the coherence ratio as well as the brightness ratio, the accuracy increased from 0.71 to 0.75. While the recall of non-flooded DS fell slightly due to increased false alarms, this was more than offset by the increase in recall of deep-flooded DS, and the use of coherence appears to have been beneficial for this wider classification also. However, the overall urban flood extent generated from DS heights proved to be only

slightly improved by the use of coherence, due to the relatively small number of DS reclassified using the coherence ratio in the deep-flooded area and their distance from the flood edge.

To the best of our knowledge, no previous publication exists of an urban flood classification method that investigates deep flooding using double scattering and interferometric coherence in conjunction with a high-resolution DSM. Our analysis provides a baseline against which improvements due to image coherence can be assessed, by comparing classification results for double scatterers with and without using the coherence ratio.

Note that our results are based on the Koriyama deep-flooded urban area, where the buildings are mostly built of brick and surrounded by asphalt. The SAR double scattering ratio depends on the materials comprising the building walls and ground surface, and the coherence ratio depends on the ground surface. We should add the caveat that the method should strictly only be applied to flooding over similar urban areas. However, as asphalt surrounding brick-built buildings is a very common urban cover, it should still be applicable to many urban areas around the world.

As stated previously, the Sentinel-1 GFM product now provides probabilistic flood extents in near real-time on a global basis.[9] However, due to the problems of detecting flooding in urban areas, these are currently masked out. The improved detection of deeper urban floods by supplementing brightness ratio with interferometric coherence could be an important step in the process of automating the detection of urban flooding as an aid to flood risk management.

Disclosures

The authors have no competing interests to declare.

Code and Data Availability

The S-1 data used in the study are open access,[49] as are the World Settlement Footprint data.[45] The WorldDEM data were purchased from Apollo Mapping.

Acknowledgments

This work was supported by the UK Natural Environment Research Council (NERC Grant No. NE/X019071/1, "UK EO Climate Information Service").

References

1. H. C. Winsemius et al., "Global drivers of future river flood risk," *Nat. Clim. Change* **6**, 381–385 (2015).
2. B. Tellmann et al., "Satellite imaging reveals increased proportion of population exposed to floods," *Nature* **596**(7870), 80–86 (2021).
3. M. Pitt, "Learning lessons from the 2007 floods," U.K. Cabinet Office Report, 2008, http://archive.cabinetoffice.gov.uk/pittreview/thepittreview.html.
4. J. Garcia-Pintado et al., "Satellite-supported flood forecast in river networks: a real case study," *J. Hydrol.* **523**, 706–724 (2015).
5. E. S. Cooper et al., "Observation operators for assimilation of satellite observations in fluvial inundation forecasting," *Hydrol. Earth Syst. Sci.* **23**, 2541–2559 (2019).
6. H. Hooker et al., "A multi-system comparison of forecast flooding extent using a scale-selective approach," *Hydrol. Res.* **54**(10), 1115–1133 (2023).
7. H. Hooker et al., "Assessing the spatial spread–skill of ensemble flood maps with remote-sensing observations," *Nat. Hazards Earth Syst. Sci.* **23**(8), 2769–2785 (2023).
8. H. Hooker et al., "Spatial scale evaluation of forecast flood inundation maps," *J. Hydrol.* **612**, 128170 (2022).
9. "GFM: GloFas Global Flood Monitoring (GFM)," 2021, https:/www.globalfloods.eu/technical-information/glofas-gfm/.
10. S. Grimaldi et al., "Sensing-derived water extent and level to constrain hydraulic flood forecasting models: opportunities and challenges," *Surv. Geophys.* **37**, 977–1034 (2016).
11. E. Nemni et al., "Fully convolutional neural network for rapid flood segmentation in Synthetic Aperture Radar imagery," *Remote Sens.* **12**, 2532 (2020).
12. D. C. Mason et al., "Flood detection in urban areas using TerraSAR-X," *IEEE. Trans. Geosci. Remote Sens.* **48** (2), 882–894 (2010).
13. D. C. Mason et al., "Near real-time flood detection in urban and rural areas using high resolution Synthetic Aperture Radar images," *IEEE. Trans. Geosci. Remote Sens.* **50**(8), 3041–3052 (2012).

14. D. C. Mason et al., "Detection of flooded urban areas in high resolution Synthetic Aperture Radar images using double scattering," *Int. J. Appl. Earth Obs. Geoinf.* **28C**, 150–159 (2014).
15. M. Tanguy et al., "River flood mapping in urban areas combining RADARSAT-2 and flood return period data," *Remote Sens. Environ.* **198**, 442–459 (2017).
16. L. Giustarini et al., "A change detection approach to flood mapping in urban areas using TerraSAR-X," *IEEE. Trans. Geosci. Remote Sens.* **51**(4), 2417–2430 (2013).
17. P. Iervolini et al., "Flooding water depth estimation with high-resolution SAR," *IEEE Trans. Geosci. Rem. Sens.* **53**(5), 2295–2307 (2015).
18. D. C. Mason, S. L. Dance, and H. L. Cloke, "Floodwater detection in urban area using Sentinel-1 and WorldDEM data," *J. Appl. Remote Sens.* **15**(3), 032003 (2021).
19. Z. Wang et al., "Combining SAR images with land cover products for rapid urban flood mapping," *Front. Environ. Sci.* **10**, 973192 (2022).
20. M.T. Islam and Q. Meng, "An exploratory study of Sentinel-1 SAR for rapid urban flood mapping on Google Earth Engine," *Int. J. App. Earth Obs. Geoinf.* **113**, 103002 (2022).
21. Q. Yang et al., "Promoting SAR-based urban flood mapping with adversarial generative network and out of distribution detection," in *IGARSS*, pp. 2336–2338 (2023).
22. L. Pulvirenti et al., "Use of SAR data for detecting floodwater in urban and agricultural areas: the role of interferometric coherence," *IEEE Trans. GeoSci. Remote Sens.* **54**(3), 1532–1544 (2016).
23. M. Chini et al., "Sentinel-1 InSAR coherence to detect floodwater in urban areas: Houston and Hurricane Harvey as a test case," *Remote Sens.* **11**, 107 (2019).
24. Y. Li et al., "Urban flood mapping using SAR intensity and interferometric coherence via Bayesian network fusion," *Remote Sens.* **11**, 2231–2252 (2019).
25. Y. Li, S. Martinis, and M. Wieland, "Urban flood mapping with an active self-learning convolutional neural network based on TerraSAR-X intensity and interferometric coherence," *ISPRS J. Photogramm. Remote Sens.* **152**, 178–191 (2019).
26. I. Olthof and N. Svacina, "Testing urban mapping approaches from satellite and in-situ data collected during 2017 and 2019 events in Eastern Canada," *Remote Sens.* **12**, 3141 (2020).
27. A. Bioretsita, N. Hayati, and M. G. R. Ngurawan, "Integrating InSAR coherence and backscattering for identification of temporary surface water, case study: South Kalimantan flooding, Indonesia," *Int. Arch. Photogramm. Rem. Sens.* **XLIII-B3**, 33–39 (2022).
28. H. Zhang et al. "An urban flooding index for unsupervised inundated urban area detection using Sentinel-1 polarimetric SAR images," *Remote Sens.* **13**, 4511 (2021).
29. R. Pelich et al. "Mapping floods in urban areas from dual-polarization InSAR coherence data," *IEEE Geosci. Remote Sens. Lett.* **19**, 4018405 (2022).
30. J. Zhao et al. "Urban-aware U-net for large-scale urban flood mapping using multitemporal Sentinel-1 intensity and interferometric coherence," *IEEE TGARS* **60**, 4209121 (2022).
31. N. G. Sorboni et al., "Urban flood mapping using Sentinel-1 and RADARSAT constellation mission image and convolutional Siamese network," *Nat. Hazards* **120**, 5711–5742 (2024).
32. Y. N. Lin et al., "Urban flood detection with Sentinel-1 multi-temporal Synthetic Aperture Radar (SAR) observations in a Bayesian Framework: a case study for Hurricane Matthew," *Remote Sens.* **11**, 1778 (2019).
33. L. Pulvirenti et al. "Flood detection in urban areas: analysis of time series of coherence data in stable scatterers," in *Proc. IGARSS*, pp. 9745–9747 (2019).
34. L. Pulvirenti, M. Chini, and N. Pierdicca, "InSAR multitemporal data over persistent scatterers to detect floodwater in urban areas: a case study in Beletweyne, Somalia," *Remote Sens.* **13**, 37 (2021).
35. L. Moya et al. "Learning from the 2018 Western Japan heavy rains to detect floods during the 2019 Hagibis Typhoon," *Remote Sens.* **12**(14), 2244 (2020).
36. G. Franceschetti et al., "SAR raw signal simulation for urban structures," *IEEE Trans. Geosci. Remote Sens.* **41**(9), 1986–1995 (2003).
37. G. Franceshetti, A. Iodice, and D. Riccio, "A canonical problem in electromagnetic backscattering from buildings," *IEEE Trans. Geosci. Remote Sens.* **40**(8), 1787–1801 (2002).
38. D. C. Mason, S. L. Dance, and H. L. Cloke, "Towards improved urban flood detection using Sentinel-1: dependence of the ratio of post- to pre-flood double scattering cross-sections on building orientation," *J. Appl. Remote Sens.* **17**(1), 016507 (2023).
39. M. Ohki et al., "Flood area detection using PALSAR-2 Amplitude and coherence data: the case of the 2015 heavy rainfall in Japan," *IEEE JSTARS* **12**, 2288–2298 (2019).
40. JBA, "Typhoon Hagibis: JBA risk management event response, 14 October 2019," 2019, https://www.jbarisk.com/products-services/event-response/typhoon-hagibis/.
41. Synspective, "Analysing the Abukuma River Flood (2019) with flood damage assessment," (2020), https://synspective.com/usecase/2020/fda1/ (accessed 03/04/2024).
42. Geospatial Information Authority of Japan, "Information about Typhoon No. 19," (2019), https://www.gsi.go.jp/BOUSAI/R1.taihuu19gou.html.

43. Guardian, (2019), https://www.theguardian.com/world/gallery/2019/oct/14/the-aftermath-of-typhoon-hagibis-in-pictures.
44. ESA, (2021), https://step.esa.int/docs/tutorials/S1TBX%20TOPSAR%20Interferometry%20with%20Sentinel-1%20Tutorial_v2.pdf.
45. ESA, (2019), https://urban-tep.eu/#!.
46. L. S. Davis, "A survey of edge detection techniques," *Comput. Graphics Image Process.* **4**(3), 248–270 (1975).
47. F. S. Nahm, "Receiver operating characteristic curve: overview and practical use for clinicians," *Korean J. Anesthesiol.* **75**(1), 25–36 (2022).
48. E. Stephens, G. Schumann, and P. D. Bates, "Problems with binary pattern measures for flood model evaluation," *Hydrol. Process.* **28**, 4928–4937 (2014).
49. "Copernicus data space ecosystem," (2023), https://dataspace.copernicus.eu/.

David C. Mason is a post-doctoral research assistant at the National Centre for Earth Observation in the Department of Meteorology at the University of Reading, United Kingdom. He obtained a BSc and PhD degrees in physics from Imperial College, University of London. His current research interest is the use of remote sensing in hydrology, in particular using SAR flood extents for emergency flood relief management and improved flood inundation forecasting.

Sarah L. Dance is a professor of Data Assimilation at the University of Reading, United Kingdom, jointly held in the Department of Mathematics and Statistics and the Department of Meteorology. She completed her PhD in the Division of Applied Mathematics at Brown University, United States, in 2002. She is the divisional director of Data Assimilation for the National Centre for Earth Observation and conducts data assimilation research with applications in meteorology and hydrology.